

Controllable crystal restructuring in MXene by electron irradiation

H. Zhang,^{1,2*} T. Hu,³ W. Sun,⁴ M.M. Hu,¹ R.F. Cheng,¹ X.H. Wang^{1*}

¹Shenyang National Laboratory for Materials Science, Institute of Metal Research, Chinese Academy of Sciences, 72 Wenhua Road, Shenyang 110016, China

²Energy Geoscience Division, Lawrence Berkeley National Laboratory, CA 94720, USA

³Institute for Materials Science and Devices, Suzhou University of Science and Technology, Suzhou 215009, China

⁴Nano and Heterogeneous Materials Center, Nanjing University of Science and Technology, Nanjing 210094, China

Recent decades have witnessed the breakthroughs in utilizing electron beams as the smallest tools to tailor materials. Whereas, the manipulation of atoms in a controllable manner by the electron beams is a long-time challenge due to the random nature of atom-knock-on. Here, we show that electron irradiation can controllably manipulate atoms in newly-developed MXene multilayers. The multilayers consist of many few-atom-thick transition metal carbide slabs that are terminated with hydroxyl and O functional groups on each slab. Upon electron irradiation, the H atoms of the hydroxyl are knocked off, creating cation traps surrounded by dangling O confined in a nano-sized slit. Simultaneously, the transition metal atoms partially struck away from the carbide slabs migrate into the cation traps periodically, resulting in crystal restructuring. Crystal restructuring is versatile for various MXenes and dramatically improves the electric conductivity and lessens the anisotropy, holding significant implications in engineering MXenes at the atomic scale.

INTRODUCTION

Beyond the detrimental effect of electron irradiation on materials, the electron beam has been used to tailor their structure and property at various length scales (1). Maybe one of the most impressive examples is electron-beam lithography for fabrication at the nanometer scale (2). Recent decades' developments in transmission electron microscope make it possible to use ultra-small electron probes as a versatile tool to tailor the structure and property of low-dimensional materials at a scale down to single atoms (3–5). It has been demonstrated that the electron probe could be used to drill nanopores, sculpture (6) and weld (7) nanowire, induce phase transformation (8, 9) and even manipulate the vacancies and doping atoms (10, 11). Irradiating materials with electrons may also bring in structural reorganization like crystallization (12) and amorphization (13). However, controllable crystal restructuring has rarely been implemented due to the uncontrollable nature of the atom-knock-on. Here we report a controllable and irreversible crystal restructuring method at the atomic scale in MXenes.

MXenes, of the formula $M_{n+1}X_nT_x$, where M is a transition metal, X is C or N, and T_x denotes surface functional groups, are a relatively young class of two-dimensional solids and have been used as electromagnetic interference shielding (14), molecular sieving (15), catalyst (16), photoabsorber (17), biosensor (18), electrochemical energy

*Corresponding author. *Email address*: huizhang_issac@hotmail.com (H. Zhang), wang@imr.ac.cn (X.H. Wang).

storage materials (19–21) and laser technology (22). MXenes are mostly produced by etching the A-group (generally group III A and IV A elements) layers from the MAX phases (23, 24) by aqueous HF, and subsequent sonication. The surfaces of MX slabs are typically decorated by O, OH and F functional groups. It is demonstrated that electron irradiation could trigger the migration of M atoms onto the surface of MXenes (25) and facilitate the homoepitaxial growth of new MXenes at 500 °C (26) on the MXene single sheets, providing a new bottom-up synthesis method for MXenes. Noteworthily, only a small portion of the exfoliated MXene are atomically thin, most of the products are generally quasi-two-dimensional multilayers (Fig. S1A,B) with functional groups comprising H/O/F re-filled the atomic-scale gaps between MX slabs. Manipulating the structure of MXene multilayers is therefore of more scientific and technological importance. In this paper, we use the MXene multilayers as benchmark materials to demonstrate the proof-of-concept crystal restructuring by electron probe.

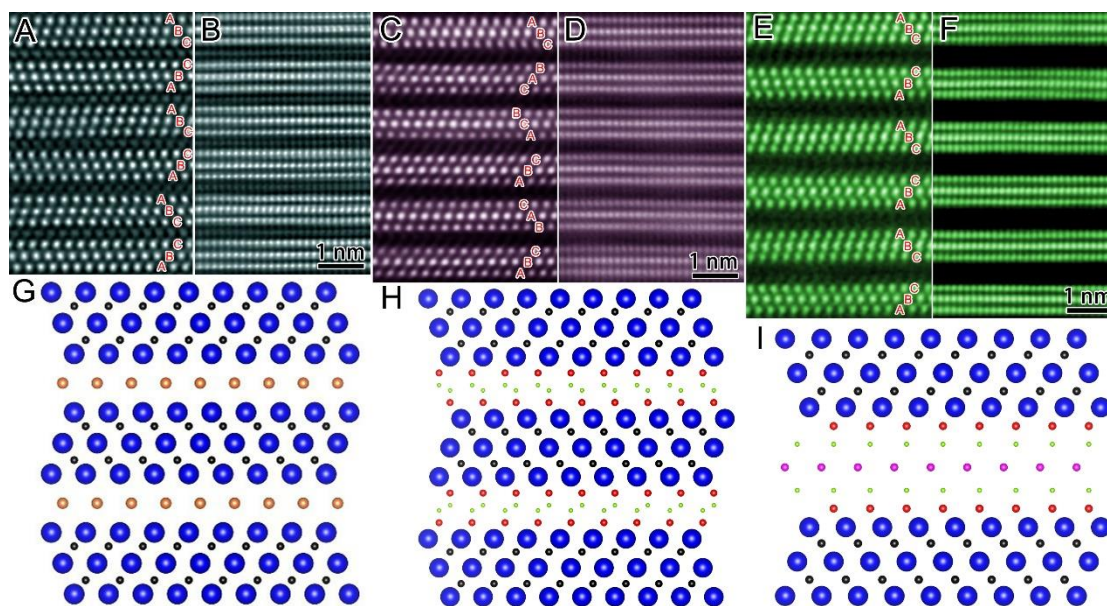


Fig. 1. Structures of Ti_3AlC_2 and pristine Ti_3C_2 -MXene. Atomic-resolution HAADF-STEM images of (A,B) Ti_3AlC_2 , (C,D) $Ti_3C_2T_x$ and (E,F) NH_3 - $Ti_3C_2T_x$. Zone axes in (A,C,E) and (B,D,F) are $\langle 11\bar{2}0 \rangle$ and $\langle 10\bar{1}0 \rangle$ respectively. The intensity of an atomic column in the HAADF-STEM image is approximately proportional to the square of the average atomic number of the column (22 for Ti, 13 for Al, 6 for C, 8 for O, 9 for F, 1 for H), the bright dots are therefore Ti columns. The stacking sequence of Ti is labeled as A/B/C in (A,C,E). The atomic model for Ti_3AlC_2 , $Ti_3C_2T_x$ and NH_3 - $Ti_3C_2T_x$ along $\langle 11\bar{2}0 \rangle$ are illustrated in (G), (H) and (I) respectively, with Ti, Al, C, O and H being denoted by blue, yellow, black, red and green balls. F is not illustrated for brevity due to its low concentration. Purple balls in (I) illustrate the atoms (N, O) introduced into the T_x slabs by NH_3 treatment.

RESULTS AND DISCUSSION

Pristine structure of MXenes. As the most intensively investigated MXene so far, Ti_3C_2 -MXene is often prepared by means of selective chemical etching Al atomic layers from the layered ternary carbide precursor, Ti_3AlC_2 . Fig. 1A,B show the high-angle annular dark-field scanning transmission electron microscopy (HAADF-STEM) images of Ti_3AlC_2 demonstrating a sandwich structure of Ti_3C_2 slabs (bright contrast) and Al layers (dim contrast). At the expense of removing the Al layers, the Ti_3C_2 matrix slabs are spontaneously terminated by functional groups (24). We therefore refer the as-prepared Ti_3C_2 -MXene as $Ti_3C_2T_x$ with T_x standing for the functional groups. The nominal composition determined by electron energy-loss spectroscopy (EELS) is Ti : C : O : F = 3 : 1.8 : 2.1 : 0.6, as shown in Fig. S2. O exists as the form of hydroxyl and

–O functional groups (Fig. S3). Due to the surface functionalization of the Ti_3C_2 slabs, the c lattice parameter (c -LP) of $\text{Ti}_3\text{C}_2\text{T}_x$ is somewhat dilated to 19.58 Å, which is 8% larger than that of Ti_3AlC_2 precursor (Fig. S1C). By annealing $\text{Ti}_3\text{C}_2\text{T}_x$ in NH_3 atmosphere, referred to as $\text{NH}_3\text{-Ti}_3\text{C}_2\text{T}_x$ hereafter, N/O-containing groups were introduced into the gap between the Ti_3C_2 slabs (Fig. S4). The nominal composition of $\text{NH}_3\text{-Ti}_3\text{C}_2\text{T}_x$ is $\text{Ti} : \text{C} : \text{O} : \text{N} : \text{F} = 3 : 1.5 : 3 : 0.16 : 0.6$ (Fig. S4) with the c -LP further increased to 24.52 Å. The change in c -LP is straightforwardly demonstrated by the shift of (0002) peak towards lower angles in the XRD patterns (Fig. S1C).

The atomic-resolution images demonstrate definitely that the thickness of Ti_3C_2 slabs in $\text{Ti}_3\text{C}_2\text{T}_x$ (Fig. 1C,D) and $\text{NH}_3\text{-Ti}_3\text{C}_2\text{T}_x$ (Fig. 1E,F) are basically the same as that in Ti_3AlC_2 , 4.90 Å, while c -LP changes significantly. The change of c -LP stems from the difference in the spacing of two adjacent Ti_3C_2 slabs, which is 4.40 Å, 4.80 Å and 6.80 Å in Ti_3AlC_2 , $\text{Ti}_3\text{C}_2\text{T}_x$ and $\text{NH}_3\text{-Ti}_3\text{C}_2\text{T}_x$ respectively. In addition to the change in interlayer spacing, the relative stacking of Ti_3C_2 slabs is altered. In Ti_3AlC_2 , two adjacent Ti_3C_2 slabs have twin orientation relationship. Whereas such twin orientation is altered in $\text{Ti}_3\text{C}_2\text{T}_x$ where Ti_3C_2 slabs are randomly shifted by $1/3\langle 10\bar{1}0 \rangle$ (Fig. 1C). Interestingly, the twin orientation is restored in $\text{NH}_3\text{-Ti}_3\text{C}_2\text{T}_x$ (Fig. 1E) where the Ti_3C_2 slabs are head-to-head stacked. Atomic configurations illustrating the stackings are provided in Fig. 1G,H,I.

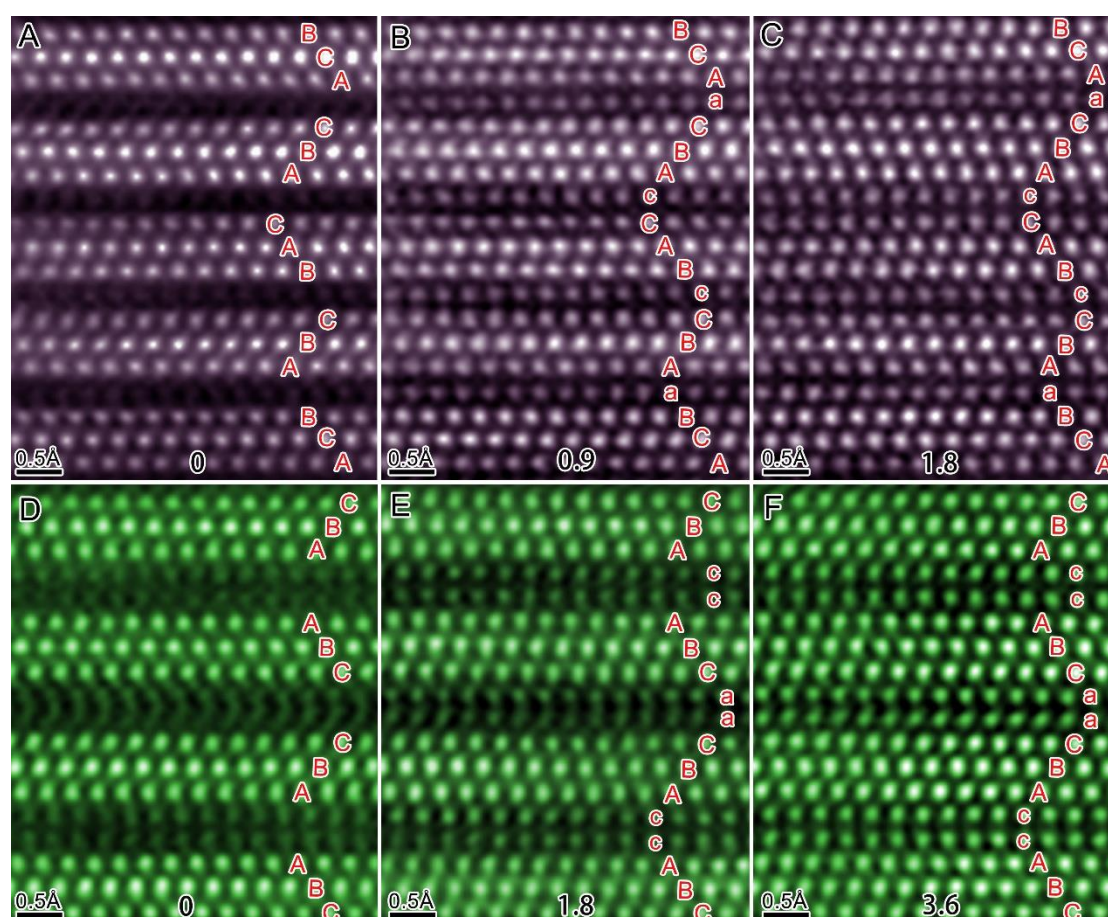


Fig. 2. Electron irradiation induced contrast change. Atomic-resolution HAADF-STEM images of one region in (A–C) $\text{Ti}_3\text{C}_2\text{T}_x$ and (D–F) $\text{NH}_3\text{-Ti}_3\text{C}_2\text{T}_x$ with the irradiation of electron beam. Irradiation time (in ms) is provided at the bottom of each image. The calculation for irradiation time is detailed in the Supplementary Note. The unavoidable and not-in-purpose irradiation time for the sample and microscope alignment is not included in the irradiation time. Electron dose rate is estimated to be

$1.25 \times 10^9 \text{ e}^-/\text{\AA}^2\text{s}$ at 300 kV. The capital (A/B/C) and lowercase (a/c) letters denote the stacking sequence of Ti in Ti_3C_2 and T_x slabs, respectively.

Electron-induced atom-repartition. Fig. 2A–C present the HAADF–STEM images of one region in Ti_3C_2T_x after irradiated for 0, 0.6, 1.2 and 1.8 ms with an electron dose rate of $1.25 \times 10^9 \text{ e}^-/\text{\AA}^2\text{s}$ at 300 kV. The nearly invisible T_x slabs exhibit appreciable intensities after 0.6 ms exposure of electrons, indicating that some Ti atoms in the Ti_3C_2 slabs migrate into the T_x slabs and periodically occupy the atop sites with respect to the outer Ti atoms in one of the two adjacent Ti_3C_2 slabs. Fig. 2D–F demonstrate the irradiation results of $\text{NH}_3\text{-Ti}_3\text{C}_2T_x$. The enhancement of brightness of T_x slabs due to the redistribution of Ti is prominent as well but less evident than that in Ti_3C_2T_x . The intensity of an atomic column in HAADF–STEM image is roughly in proportion to Z^2 (Z is the average atomic number) (27, 28). The accommodation sites for the coming Ti atoms in $\text{NH}_3\text{-Ti}_3\text{C}_2T_x$ are twice those in Ti_3C_2T_x as evidenced by the two bright atomic layers between the Ti_3C_2 slabs (Fig. 2E,F), the average intensity ratio between T_x and Ti_3C_2 slabs, I_T/I_M in Ti_3C_2T_x is expected to be four times that in $\text{NH}_3\text{-Ti}_3\text{C}_2T_x$ for the same Ti out-migration rate. Agreeing with this analysis, the increase of I_T/I_M with irradiation dose in Ti_3C_2T_x is averagely 5 times faster than that in $\text{NH}_3\text{-Ti}_3\text{C}_2T_x$. This interesting difference in I_T/I_M could be further dynamically confirmed in Supplementary V1. After 1.8 ms irradiation for Ti_3C_2T_x and 6.0 ms irradiation for $\text{NH}_3\text{-Ti}_3\text{C}_2T_x$, the average intensities of T_x slabs reach $\sim 80\%$ of those of Ti_3C_2 slabs.

To more quantitatively demonstrate the difference in irradiation effect between these two MXenes, Fig. 3A plots the I_T/I_M as a function of irradiation dose, solid spheres. The non-zero value of I_T/I_M at the beginning is due to the unavoidable electron irradiation during the sample and microscope alignment. To estimate the Ti vacancy (V_{Ti}) concentration in the Ti_3C_2 slabs caused by the Ti-repartition between the Ti_3C_2 and T_x slabs, HAADF–STEM image simulations were employed with the imaging conditions used to obtain the dose dependence of I_T/I_M . After that, the V_{Ti} under each electron dose is determined by comparing the simulated and experimental I_T/I_M . Fig. 3B,D present the composite images of experimental and simulated (inset) HAADF–STEM images of $V_{\text{Ti}} \approx 0.2$ in Ti_3C_2T_x and $V_{\text{Ti}} \approx 0.3$ in $\text{NH}_3\text{-Ti}_3\text{C}_2T_x$ with the model illustrated in Fig. 3C,E respectively. The models were constructed on the base of the first-principles calculations detailed latter. Remarkable consistency could be observed except those marked by arrows wherein the intensity of Ti columns are weaker than others in the Ti_3C_2 slabs, indicating more V_{Ti} therein. The nonhomogeneous V_{Ti} is due to the damage of Ti_3C_2 during the etching (29) rather than the electron irradiation. The irradiation would not change the relative V_{Ti} concentration ratio between the outer and inner Ti columns in Ti_3C_2 slabs as suggested in Fig. S5. The calculated V_{Ti} formation energies in the inner Ti columns is $\sim 130\%$ higher than that in the outer Ti columns. Therefore, it is much easier to form a V_{Ti} in the outer than the inner Ti column (29). The outer Ti atoms in the Ti_3C_2 slabs migrate out first into the functional group slabs but the produced V_{Ti} therein will be compensated by the inner Ti atoms very quickly so that no difference in V_{Ti} caused by electron beam irradiation could be detected (Fig. S5). As shown in Fig. 3A, 22% and 32% V_{Ti} were produced in the Ti_3C_2 slabs of Ti_3C_2T_x and $\text{NH}_3\text{-Ti}_3\text{C}_2T_x$ after $2.1 \times 10^6 \text{ e}^-/\text{\AA}^2$ and $7.5 \times 10^6 \text{ e}^-/\text{\AA}^2$ irradiation, resulting in a I_T/I_M of 0.8. Notably, despite the tremendous repartition of Ti between Ti_3C_2 and T_x slabs, the stacking manner of the adjacent Ti_3C_2 slabs remain unchanged as shown in Fig. 2A–F. The newly coming Ti atoms reside the atop sites of the far Ti layers in the adjacent Ti_3C_2 slabs resulting in a stacking sequence of ABCaCBaCABC in Ti_3C_2T_x and

ABCaaCBAccABC in $\text{NH}_3\text{-Ti}_3\text{C}_2\text{T}_x$, where the capital and lowercase Roman letters denote the stacking of Ti atoms in the Ti_3C_2 and T_x slabs. It is worth pointing out that the ordered stacking sequence in $\text{Ti}_3\text{C}_2\text{T}_x$ is extremely confined within two or three Ti_3C_2 slabs due to the turbostratic stacking nature compared to that of $\text{NH}_3\text{-Ti}_3\text{C}_2\text{T}_x$ (Fig. S1D,E).

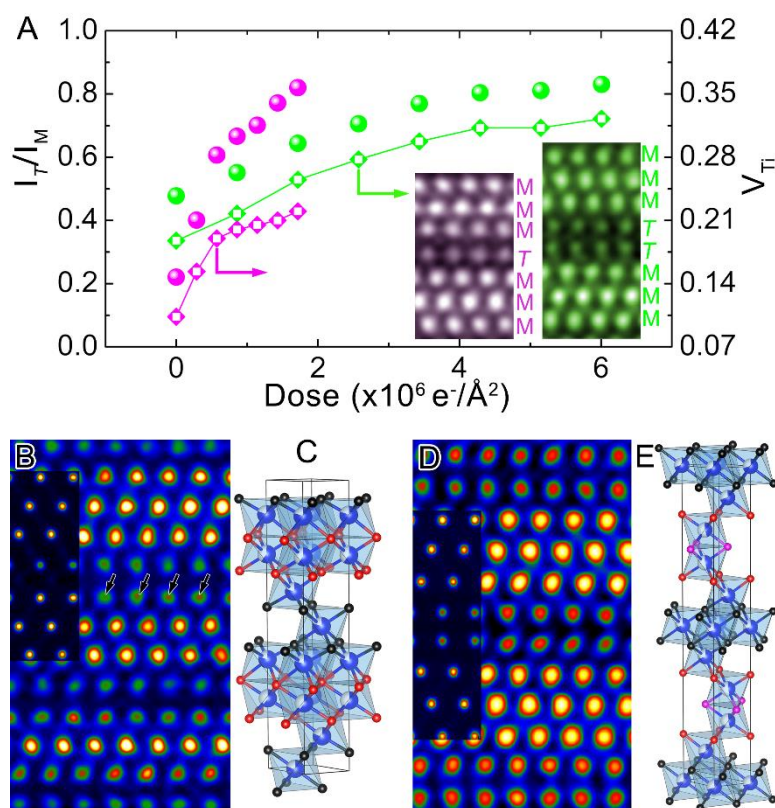


Fig. 3. Concentration of Ti vacancy. (A) Evolution of I_T/I_M and V_{Ti} in Ti_3C_2 slabs with the electron dose in $\text{Ti}_3\text{C}_2\text{T}_x$ (pink) and $\text{NH}_3\text{-Ti}_3\text{C}_2\text{T}_x$ (green). Insets show M and T layers in $\text{Ti}_3\text{C}_2\text{T}_x$ (left) and $\text{NH}_3\text{-Ti}_3\text{C}_2\text{T}_x$ (right) used for intensity calculation, which is performed on non-filtered images. (B,D) Composite images of experimental and simulated HAADF-STEM images of $V_{\text{Ti}} \approx 0.2$ in $\text{Ti}_3\text{C}_2\text{T}_x$ and $V_{\text{Ti}} \approx 0.3$ in $\text{NH}_3\text{-Ti}_3\text{C}_2\text{T}_x$. The images are presented with a temperature color-scale. Arrows in (B) mark the Ti atomic columns with lower intensities than those of the below two Ti layers in the same Ti_3C_2 slab. (C,E) Crystal structure used for the simulation in (B,D). Ti, C, O and V_{Ti} are denoted by blue, black, red and white balls. The blue and white balls are overlapped to illustrate the partial occupancy of Ti. Purple balls in (E) illustrate the atoms (N, O) introduced into T_x slab by NH_3 treatment. F atoms are not shown for brevity due to its low concentration. H atoms are believed to be removed by electron irradiation because of its low atomic mass.

The electron-beam-assisted crystal restructuring was observed in $\text{Nb}_4\text{C}_3\text{-MXene}$ and $(\text{Ti}_{0.5}\text{Nb}_{0.5})_2\text{C-MXene}$ as well (Fig. S6) and could be easily realized at 80 kV (Fig. S7). Three features can be summarized for the crystal restructuring. First, the out-hopped Ti atoms prefer to reside in the T_x slabs rather than the surface (Supplementary V2), which is in stark contrast to MXene single layer (25, 26). Second, it is irreversible. Ti atoms migrated out into the T_x slabs never go back to where they were, the Ti_3C_2 slabs, even after one week (Fig. S8). Finally, the restructuring process is highly dose-dependent, as

shown in Fig. 3A.

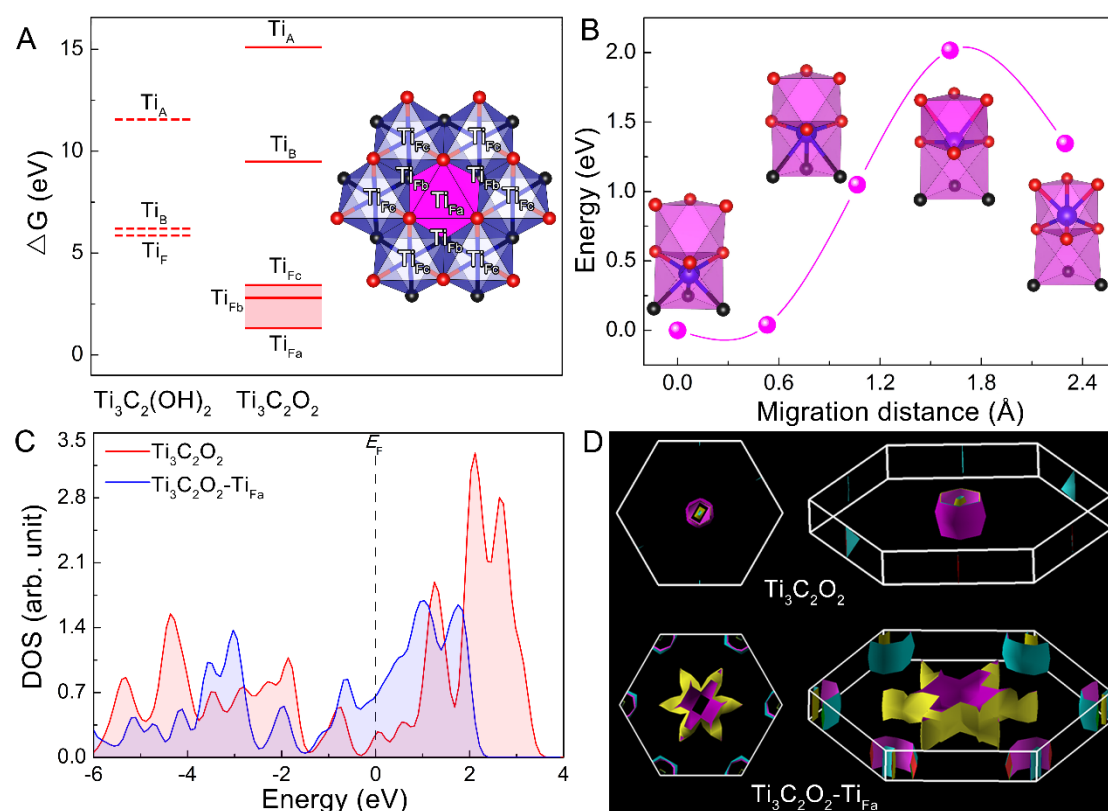


Fig. 4. Mechanism and influence of Ti migration into the functional group slabs. (A) Gibbs energy differences (ΔG) of Ti migration into a vacuum (Ti_A), bulk Ti (Ti_B) or functional group slabs (Ti_F , Ti_{Fa} , Ti_{Fb} , Ti_{Fc}) in $\text{Ti}_3\text{C}_2(\text{OH})_2$ (dashed lines) and $\text{Ti}_3\text{C}_2\text{O}_2$ (solid lines) MXene with respect to the defect free structures. For simplicity, only the lowest-energy configuration of Ti hopped into the functional group slabs in $\text{Ti}_3\text{C}_2(\text{OH})_2$, Ti_F , is illustrated. The corresponding structure is shown in Fig. S9A. One Ti atom in the octahedron highlighted in pink hops into the functional group slab of $\text{Ti}_3\text{C}_2\text{O}_2$ and resides at one of the three possible nonequivalent sites (Ti_{Fa} , Ti_{Fb} and Ti_{Fc}) above the O layers as illustrated by the projection along [0001] in the inset. The $\text{C}_3\text{-Ti-O}_3$ coordination polyhedrons are highlighted, where black and red balls are C and O atoms respectively. Ti atoms in the Ti_3C_2 slab are not shown for a clear presentation. (B) Energy barrier of Ti migration to Ti_{Fa} site in $\text{Ti}_3\text{C}_2\text{O}_2$. The insets show the configurations of one Ti (blue ball) in the two octahedrons formed by three C and three O (lower) and six O (upper). (C) DOS of Ti normalized by Ti atom numbers. (D) Fermi surfaces of $\text{Ti}_3\text{C}_2\text{O}_2$ and $\text{Ti}_3\text{C}_2\text{O}_2\text{-Ti}_{Fa}$ MXenes. In $\text{Ti}_3\text{C}_2\text{O}_2\text{-Ti}_{Fa}$ configuration, the Ti_{Fa} sites are occupied by Ti atoms.

To uncover the mechanism and influence of Ti-repartition, density functional theory (DFT) calculations were employed for the most intensively investigated Ti_3C_2T_x . In Ti_3C_2T_x , hydroxyl and $-\text{O}$ are the predominant components of the functional group slabs (Fig. S3). Our previous calculations indicate that the Bernal configuration is energetically more favorable than the simple hexagonal configuration (30), which is remarkably consistent with the HAADF-STEM images in Fig. 1C,D. Therefore, the Bernal configuration was used for the DFT calculation. The formation energy of V_{Ti} for the outer and inner Ti layers in the Ti_3C_2 slabs are ~ 5.9 eV and ~ 7.5 eV. The maximum energy transferred to a Ti atom from 300 kV electron beam is estimated to be 17.7 eV using the model in Ref. (31), which is sufficient to generate V_{Ti} in the outer Ti layers first and then the inner Ti layers (32). The question is where the out-hopped Ti atoms go? Fig. 4A plots the energy penalty of various Ti hopped configurations. Ti hopping into vacuum (Ti_A), into the functional group slabs (Ti_F , Fig. S9A) or forming bulk Ti

(Ti_B) results in an energy increase of 11.50 eV, 5.39 eV and 5.90 eV compared to the perfect structure, indicating the hopped Ti atoms are prone to stay within the functional group slabs of Ti₃C₂(OH)₂. It is worth noting that H atoms should be knocked out from hydroxyl in Ti₃C₂(OH)₂ because of its low atomic mass under the electron beam irradiation. Similarly, calculations were also made for Ti₃C₂O₂, where the energy penalty for Ti hopping to the Ti_{Fa} site in the functional group slabs (Fig. S9B), the lowest-energy configuration, is dramatically decreased to 1.35 eV from 5.39 eV, suggesting that stay in the functional group slabs is significantly energetically favorable for the out-hopped Ti atoms and remarkably agreeing with the experimental observations (Fig. 2B,C and Fig. 3B,C). Detailed analysis of the local structure around Ti_{Fa} demonstrates that the hopped-in Ti bonds strongly with the dangling O, forming TiO₆ octahedrons. In contrast, Ti_F in Ti₃C₂(OH)₂ experiences strong repulsion from H atoms. The climbing image nudged elastic band method was used to search the migration barrier and transition state for outer Ti in the Ti₃C₂ slabs hopping to Ti_{Fa} site in Ti₃C₂O₂. As shown in Fig. 4B, the migration involves breaking Ti–C bonds and forming Ti–O bonds. The Ti atom migrates out the C₃–O₃ octahedron, gradually enters the O₃–O₃ octahedron through the hollow of three nearest O, and finally is trapped there and stabilized by forming TiO₆ octahedrons with the dangling O groups. The elongation and breaking of the strong Ti–C bonds lead to an energy barrier of 2.02 eV, which is quite small compared to the energy transferred from the irradiation electrons.

The electronic conductivity is of vital significance for the variety of energy-storing applications. With Ti hopping into the functional group slabs the energy bands above Fermi energy are prominently shifted downwards (Fig. S10). As a result, the density of states (DOS) of Ti, the major conductivity contributor (33), at the Fermi level increases by 187%, suggesting a much better electronic conduction in Ti₃C₂O₂-Ti_{Fa} (Fig. 4C). The energy bands along M–L in Ti₃C₂O₂ are non-dispersive, indicating a 2D electronic conduction character (33), while those in Ti₃C₂O₂-Ti_{Fa} are more 3D-like (Fig. S10). Correspondingly, the Fermi surface vertical to the basal plane in Ti₃C₂O₂-Ti_{Fa} is snowflakes-like and show much more projection along *c* direction comparing to the cylinder-like Fermi surface in Ti₃C₂O₂, as shown in Fig. 4D. The hopped Ti atoms increase the conductivity and lessen its anisotropy (33) of multilayer MXenes, which could facilitate their promising applications in electronic industry as energy-storing devices.

In summary, we demonstrate that MXene multilayers could be re-structured by electron beam irradiation. Under the irradiation, the loss of H provides dangling O groups and favorable periodical residing sites for the M atoms knocked out from the MX slabs. The repartition of M atoms rewrites the MXene crystal structure and the conductivity anisotropy. This intriguing approach is applicable to various MXenes with different constituent atoms and MX thickness (Ti₃C₂-MXene, Nb₄C₃-MXene, (Ti_{0.5}Nb_{0.5})₂C-MXene). It is acknowledged that the atomic spices in the functional group slabs play a significant role in the physical-chemical properties of MXenes. Our findings provide huge space to engineer the MXenes, a big emerging family of 2D materials.

MATERIALS AND METHODS

Preparation of MXenes: To avoid violent exfoliation, the porous Ti₃AlC₂ monolith was immersed in 6 mol·L⁻¹ HF aqueous solution for a week at room temperature to produce Ti₃C₂-MXene. The resulting sediment was subsequently washed several times with deionized water and followed by vacuum filtration. The filtered sample was

subsequently dried overnight at 60 °C in an oven. Nb₄C₃-MXene and (Ti_{0.5}Nb_{0.5})₂C-MXene were prepared by similar processes using 20 mol·L⁻¹ HF as etching agent. The etching time is six months and one week respectively. To prepare NH₃-Ti₃C₂T_x, 0.5 g Ti₃C₂T_x powders were put into a quartz tube furnace. The tube was purged with NH₃ twice and then heated to 400 °C at a rate of 10 °C·min⁻¹ in the 100 sccm flowing NH₃ atmosphere. After keeping for 1 h at 400 °C, the sample was cooled to room temperature under the protection of flowing NH₃.

Structural characterization. The phase component of the as-synthesized sample was examined by X-ray diffraction (XRD) (Rigaku D/max-2400, Tokyo, Japan) with Cu K α radiation. Electron transparent foils were sliced from the MXene particles perpendicular to the basal plane on FEI Nova NanoSEM 450 (FEI, Oregon, USA) equipped with a dual-beam SEM/FIB system. Selected area electron diffraction patterns were recorded on a Tecnai G² F20. HAADF-STEM images and EELS spectrums were taken on a double-C_s-corrected FEI Titan³ 80-300 operating at 300 kV and 80 kV, using a collection inner semi-angle of 64 mrad and a convergence semi-angle of 21 mrad. All the atomic-scale HAADF-STEM images were processed by masking diffraction spots in the fast Fourier transform of the original image and then back transforming using Gatan DigitalMicrographTM, unless otherwise specified. QSTEM software (34) was used to simulate the HAADF-STEM images. In the beam direction, the structure was divided into slices with an approximately equal thickness of 1 Å. To account for the thermal diffuse scattering, the frozen phonon method was used, and the results were averaged over 30 frozen phonon configurations. The microscope parameters for the imaging were used for the simulation. The collection angular range of the HAADF detector was fixed to be 64~250 mrad respectively. The Ti and O edges in the EELS spectrums are nearly unchanged (Fig. S11,12), thus the total amounts of Ti and O in the various models with different Ti vacancies in the Ti₃C₂ slabs and Ti atoms in the functional group slabs are kept the same. F is not considered in the simulation due to their low concentrations.

DFT calculation

The DFT computations were performed by using the plane-wave technique implemented in the Vienna ab initio simulation package (35). The ion-electron interaction is described with the projector augmented wave method (36). A 500 eV cutoff was used for the plane-wave basis set. The exchange-correlation energy is described by the functional of Perdew, Burke, and Ernzerhof (PBE) (37). To take long-range interaction into consideration, the PBE-D method was adopted, where dispersion interactions are introduced by using DFT-D2 method of Grimme (38). The geometry optimizations were performed by using the conjugated gradient method, and the convergence threshold was set to be 10⁻⁴ eV in energy and 0.1 eV/Å in force. A 2 × 2 × 1 supercell with one Ti hopping was used to investigate the Ti migration in MXene multilayer. The Brillouin zone was represented by Monkhorst-Pack special *k*-point mesh (39) of 11 × 11 × 1 and 3 × 3 × 1 for Ti₃C₂T_x unit cell and supercell, respectively. Furthermore, the climbing image nudged elastic band method (40) was used to determine the diffusion energy barrier and the minimum energy pathways for Ti hopping in Ti₃C₂O₂ multilayer.

Reference

1. A. V. Krasheninnikov, K. Nordlund, Ion and electron irradiation-induced effects in nanostructured materials. *J. Appl. Phys.* **107**, 071301 (2010).
2. C. Vieu, F. Carcenac, A. Pépin, Y. Chen, M. Mejias, A. Lebib, L. M. Ferlazzo, L. Couraud, H. Launois, Electron beam lithography: resolution limits and applications. *Appl. Surf. Sci.* **164**, 111–117 (2000).
3. A. V. Krasheninnikov, F. Banhart, Engineering of nanostructured carbon materials with electron or ion beams. *Nat. Mater.* **6**, 723–733 (2007).
4. T. Susi, J. C. Meyer, J. Kotakoski, Manipulating low-dimensional materials down to the level of single atoms with electron irradiation. *Ultramicroscopy* **180**, 163–172 (2017).
5. R. Mishra, R. Ishikawa, A. R. Lupini, S. J. Pennycook, Single-atom dynamics in scanning transmission electron microscopy. *MRS Bulletin* **42**, 644–652 (2017).
6. J. Lin, O. Cretu, W. Zhou, K. Suenaga, D. Prasai, K. I. Bolotin, N. T. Cuong, M. Otani, S. Okada, A. R. Lupini, J. C. Idrobo, D. Caudel, A. Burger, N. J. Ghimire, J. Yan, D. G. Mandrus, S. J. Pennycook, S. T. Pantelides, Flexible metallic nanowires with self-adaptive contacts to semiconducting transition-metal dichalcogenide monolayers. *Nat. Nanotechnol.* **9**, 436–442 (2014).
7. L. Zhang, Y. Tang, Q. Peng, T. Yang, Q. Liu, Y. Wang, Y. Li, C. Du, Y. Sun, L. Cui, F. Yang, T. Shen, Z. Shan, J. Huang, Ceramic nanowelding. *Nat. Commun.* **9**, 96 (2018).
8. P. Gao, R. Ishikawa, E. Tochigi, A. Kumamoto, N. Shibata, Y. Ikuhara, Atomic-scale tracking of a phase transition from spinel to rocksalt in lithium manganese oxide. *Chem. Mater.* **29**, 1006–1013 (2017).
9. Y. C. Lin, D. O. Dumcenco, Y. S. Huang, K. Suenaga, Atomic mechanism of the semiconducting-to-metallic phase transition in single-layered MoS₂. *Nat. Nanotechnol.* **9**, 391–396 (2014).
10. H.P. Komsa, J. Kotakoski, S. Kurasch, O. Lehtinen, U. Kaiser, A. V. Krasheninnikov, Two-dimensional transition metal dichalcogenides under electron irradiation: defect production and doping. *Phys. Rev. Lett.* **109**, 035503 (2012).
11. H.P. Komsa, S. Kurasch, O. Lehtinen, U. Kaiser, A. V. Krasheninnikov, From point to extended defects in two-dimensional MoS₂: Evolution of atomic structure under electron irradiation. *Phys. Rev. B* **88**, 035301 (2013).
12. I. Jenčič, M. W. Bench, I. M. Robertson, M. A. Kirk, Electron-beam-induced crystallization of isolated amorphous regions in Si, Ge, GaP, and GaAs. *J. Appl. Phys.* **78**, 974–982 (1995).
13. J. Kotakoski, A. V. Krasheninnikov, U. Kaiser, J. C. Meyer, From point defects in graphene to two-dimensional amorphous carbon. *Phys. Rev. Lett.* **106**, 105505 (2011).
14. F. Shahzad, M. Alhabeb, C. B. Hatter, B. Anasori, S. Man Hong, C. M. Koo, Y. Gogotsi, Electromagnetic interference shielding with 2D transition metal carbides (MXenes). *Science* **353**, 1137–1140 (2016).
15. L. Ding, Y. Wei, L. Li, T. Zhang, H. Wang, J. Xue, L.-X. Ding, S. Wang, J. Caro,

- Y. Gogotsi, MXene molecular sieving membranes for highly efficient gas separation. *Nat. Commun.* **9**, 155 (2018).
16. Z. W. Seh, K. D. Fredrickson, B. Anasori, J. Kibsgaard, A. L. Strickler, M. R. Lukatskaya, Y. Gogotsi, T. F. Jaramillo, A. Vojvodic, Two-dimensional molybdenum carbide (MXene) as an efficient electrocatalyst for hydrogen evolution. *ACS Energy Letters* **1**, 589–594 (2016).
 17. J. Xuan, Z. Wang, Y. Chen, D. Liang, L. Cheng, X. Yang, Z. Liu, R. Ma, T. Sasaki, F. Geng, Organic-base-driven intercalation and delamination for the production of functionalized titanium carbide nanosheets with superior photothermal therapeutic performance. *Angew. Chem.* **128**, 14789–14794 (2016).
 18. B. Xu, M. Zhu, W. Zhang, X. Zhen, Z. Pei, Q. Xue, C. Zhi, P. Shi, Ultrathin MXene-micropattern-based field-effect transistor for probing neural activity. *Adv. Mater.* **28**, 3333–3339 (2016).
 19. M. Ghidui, M. R. Lukatskaya, M. Q. Zhao, Y. Gogotsi, M. W. Barsoum, Conductive two-dimensional titanium carbide 'clay' with high volumetric capacitance. *Nature* **516**, 78–81 (2014).
 20. D. Er, J. Li, M. Naguib, Y. Gogotsi, V. B. Shenoy, Ti_3C_2 MXene as a high capacity electrode material for metal (Li, Na, K, Ca) ion batteries. *ACS Appl. Mater. Interfaces* **6**, 11173–11179 (2014).
 21. Y. Xia, T. S. Mathis, M.-Q. Zhao, B. Anasori, A. Dang, Z. Zhou, H. Cho, Y. Gogotsi, S. Yang, Thickness-independent capacitance of vertically aligned liquid-crystalline MXenes. *Nature* **557**, 409–412 (2018).
 22. Y. I. Jhon, J. Koo, B. Anasori, M. Seo, J. H. Lee, Y. Gogotsi, Y. M. Jhon, Metallic MXene saturable absorber for femtosecond mode-locked lasers. *Adv. Mater.* **29**, 1702496 (2017).
 23. M. Naguib, M. Kurtoglu, V. Presser, J. Lu, J. Niu, M. Heon, L. Hultman, Y. Gogotsi, M. W. Barsoum, Two-dimensional nanocrystals produced by exfoliation of Ti_3AlC_2 . *Adv. Mater.* **23**, 4248–4253 (2011).
 24. M. Naguib, V. N. Mochalin, M. W. Barsoum, Y. Gogotsi, 25th anniversary article: MXenes: a new family of two-dimensional materials. *Adv. Mater.* **26**, 992–1005 (2014).
 25. J. Palisaitis, I. Persson, J. Halim, J. Rosen, P. O. A. Persson, On the structural stability of MXene and the role of transition metal adatoms. *Nanoscale* **10**, 10850–10855 (2018).
 26. X. Sang, Y. Xie, D. E. Yilmaz, R. Lotfi, M. Alhabeab, A. Ostadhossein, B. Anasori, W. Sun, X. Li, K. Xiao, P. R. C. Kent, A. C. T. van Duin, Y. Gogotsi, R. R. Unocic, In situ atomistic insight into the growth mechanisms of single layer 2D transition metal carbides. *Nat. Commun.* **9**, 2266 (2018).
 27. D. A. Muller, Structure and bonding at the atomic scale by scanning transmission electron microscopy. *Nat. Mater.* **8**, 263–270 (2009).
 28. S. J. Pennycook, D. E. Jesson, Atomic resolution Z-contrast imaging of interfaces. *Acta Metall. Mater.* **40**, S149–S159 (1992).
 29. X. Sang, Y. Xie, M. W. Lin, M. Alhabeab, K. L. Van Aken, Y. Gogotsi, P. R. Kent, K. Xiao, R. R. Unocic, Atomic defects in monolayer titanium carbide ($Ti_3C_2T_x$) MXene.

- ACS Nano* **10**, 9193–9200 (2016).
30. T. Hu, M.M. Hu, Z.J. Li, H. Zhang, C. Zhang, J.Y. Wang, X.H. Wang, Interlayer coupling in two-dimensional titanium carbide MXenes. *Phys. Chem. Chem. Phys.* **18**, 20256–20260 (2016)
 31. R. F. Egerton, R. McLeod, F. Wang, M. Malac, Basic questions related to electron-induced sputtering in the TEM. *Ultramicroscopy* **110**, 991–997 (2010).
 32. L. H. Karlsson, J. Birch, J. Halim, M. W. Barsoum, P. O. Å. Persson, Atomically resolved structural and chemical investigation of single MXene sheets. *Nano Lett.* **15**, 4955–4960 (2015).
 33. T. Hu, H. Zhang, J. Wang, Z. Li, M. Hu, J. Tan, P. Hou, F. Li, X. Wang, Anisotropic electronic conduction in stacked two-dimensional titanium carbide. *Sci. Rep.* **5**, 16329 (2015).
 34. C. Koch, thesis, Arizona State University (2002).
 35. G. Kresse, J. Furthmüller, Efficient iterative schemes for ab initio total-energy calculations using a plane-wave basis set. *Phys. Rev. B* **54**, 11169–11186 (1996).
 36. P. E. Blöchl, Projector augmented-wave method. *Phys. Rev. B* **50**, 17953–17979 (1994).
 37. J. P. Perdew, K. Burke, M. Ernzerhof, Generalized gradient approximation made simple. *Phys. Rev. Lett.* **77**, 3865 (1996).
 38. S. Grimme, Semiempirical GGA-type density functional constructed with a long-range dispersion correction. *J. Comput. Chem.* **27**, 1787–1799 (2006).
 39. J. D. Pack, H. J. Monkhorst, "Special points for Brillouin-zone integrations"-a reply*. *Phys. Rev. B* **16**, 1748 (1977).
 40. G. Henkelman, B. P. Uberuaga, H. Jónsson, A climbing image nudged elastic band method for finding saddle points and minimum energy paths. *J. Chem. Phys.* **113**, 9901–9904 (2000).

Supplementary Materials

Controllable crystal restructuring in MXene by electron irradiation

H. Zhang,^{1,2*} T. Hu,³ W. Sun,⁴ M.M. Hu,¹ R.F. Cheng,¹ X.H. Wang^{1*}

¹Shenyang National Laboratory for Materials Science, Institute of Metal Research, Chinese Academy of Sciences, 72 Wenhua Road, Shenyang 110016, China

²Energy Geoscience Division, Lawrence Berkeley National Laboratory, CA 94720, USA

³Institute for Materials Science and Devices, Suzhou University of Science and Technology, Suzhou 215009, China

⁴Nano and Heterogeneous Materials Center, Nanjing University of Science and Technology, Nanjing 210094, China

Supplementary Note

The electron irradiation was mainly performed with a probe current ~ 40 pA. The probe diameter is estimated to be 0.8 Å. The single-frame-acquired and series-frame-acquired HAADF-STEM images were recorded with a pixel size of 0.32 Å \times 0.32 Å. The probe dose rate is calculated to be 5×10^8 e⁻/Å²s. The local dose rate on each pixel is 1.25×10^9 e⁻/Å²s. The irradiation time for each pixel in the single-frame-acquired

HAADF-STEM image t is calculated by the following equation: $t = \frac{T}{N*N*D} D = \frac{T}{N*N}$.

T is the total scanning time, N is the pixels along the scanning direction of HAADF-STEM images, and D is the dwell time per pixel. The total dose for each pixel is calculated by multiplying the local dose rate by irradiation time.

*Corresponding author. *Email address*: huizhang_issac@hotmail.com (H. Zhang), wang@imr.ac.cn (X.H. Wang).

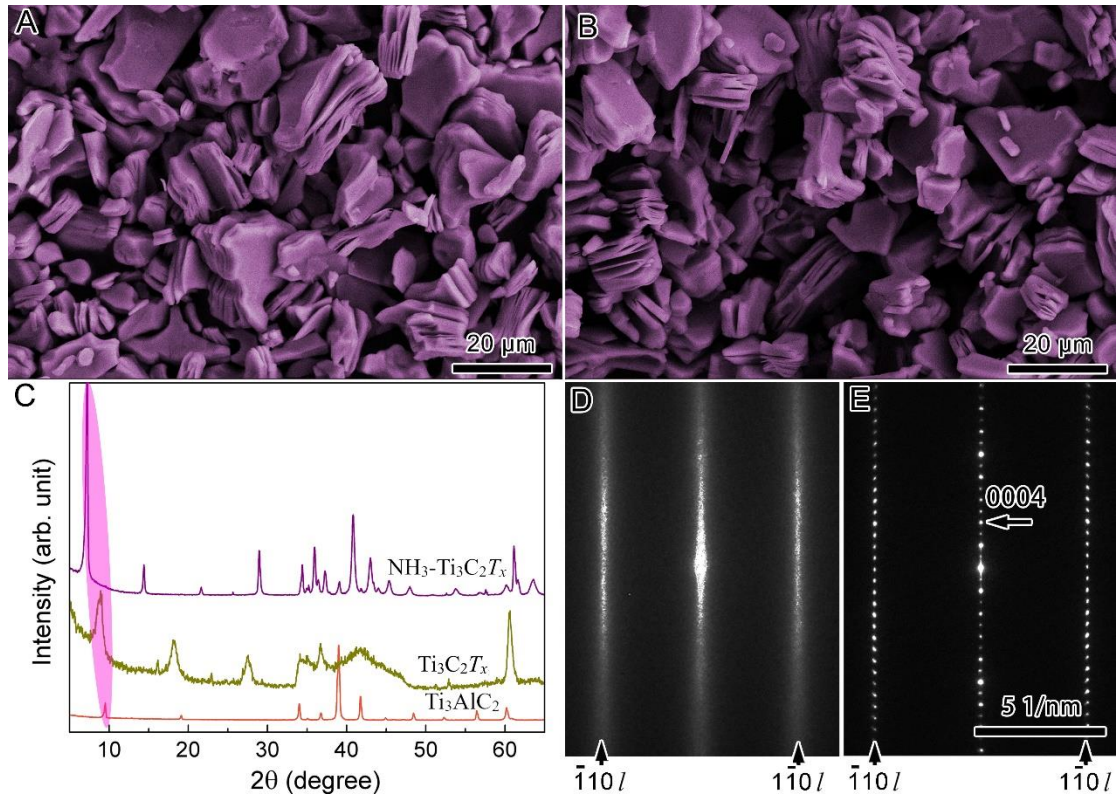


Fig. S1. Morphology and phase component of $\text{Ti}_3\text{C}_2\text{-MXene}$. Scanning electron microscopy images of (A) $\text{Ti}_3\text{C}_2\text{T}_x$, (B) $\text{NH}_3\text{-Ti}_3\text{C}_2\text{T}_x$ ($\text{Ti}_3\text{C}_2\text{T}_x$ treated with NH_3). (C) XRD patterns. For comparison, the pattern of Ti_3AlC_2 is provided. No peaks of impurities like TiO_2 and TiC were observed. The main diffraction peaks of Ti_3AlC_2 are basically inherited in $\text{Ti}_3\text{C}_2\text{T}_x$ and $\text{NH}_3\text{-Ti}_3\text{C}_2\text{T}_x$ except that the peaks of $\text{Ti}_3\text{C}_2\text{T}_x$ in the range $35^\circ\sim 45^\circ$ are not well-defined and bump-like. Compared to $\text{Ti}_3\text{C}_2\text{T}_x$, the (0002) peak of $\text{NH}_3\text{-Ti}_3\text{C}_2\text{T}_x$ is shifted to a lower angle, as shown in the shadow region. (D,E) Selected area electron diffraction patterns of $\text{Ti}_3\text{C}_2\text{T}_x$ (D) and $\text{NH}_3\text{-Ti}_3\text{C}_2\text{T}_x$ (E). The streaks in (D) caused by $(1\bar{1}0/)$ and $(\bar{1}10/)$ diffractions indicate that the carbide slabs are turbostratically stacked along the c axis. In contrast, $\text{NH}_3\text{-Ti}_3\text{C}_2\text{T}_x$ show high crystallinity, as shown in (E).

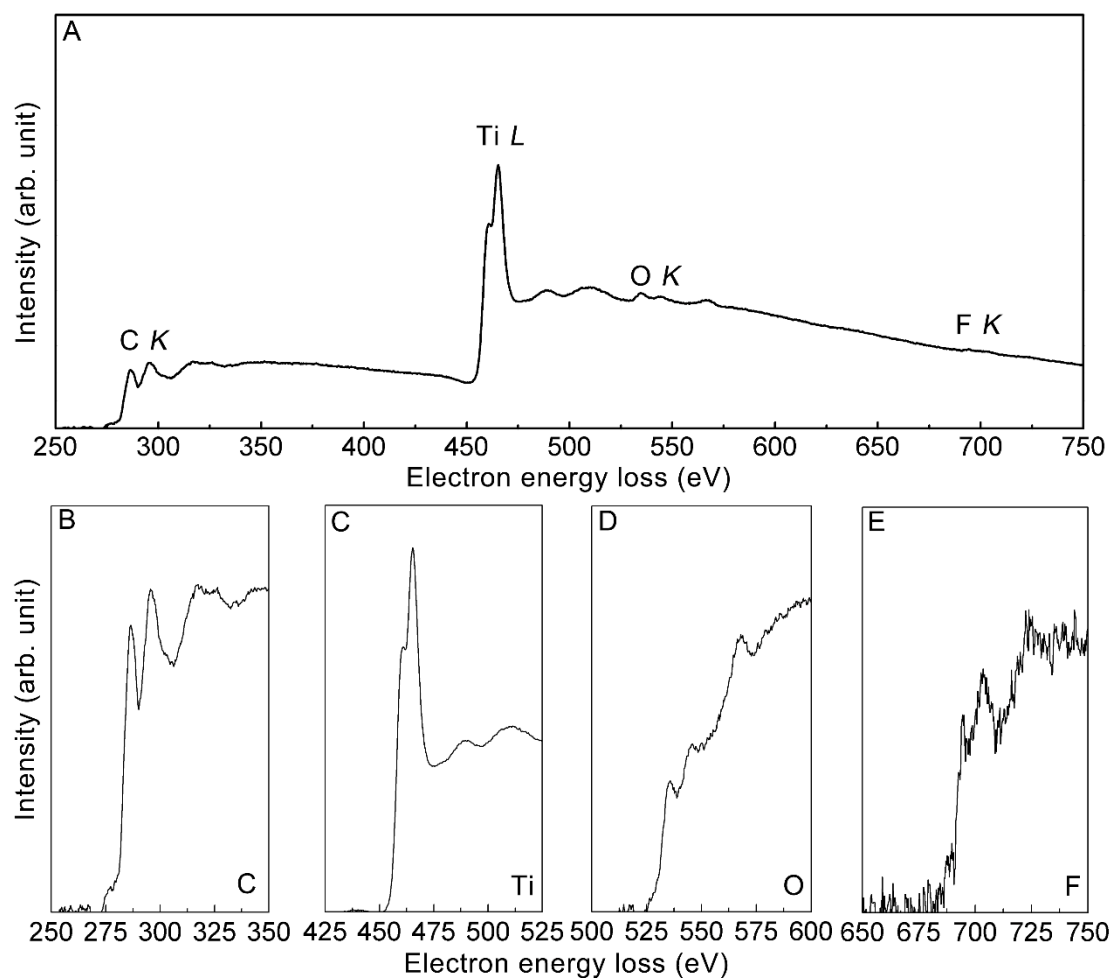


Fig. S2. EELS spectrum of $\text{Ti}_3\text{C}_2\text{T}_x$. (A) Whole spectrum with elemental peaks labeled. (B–E) Extracted edges of C, Ti, O and F.

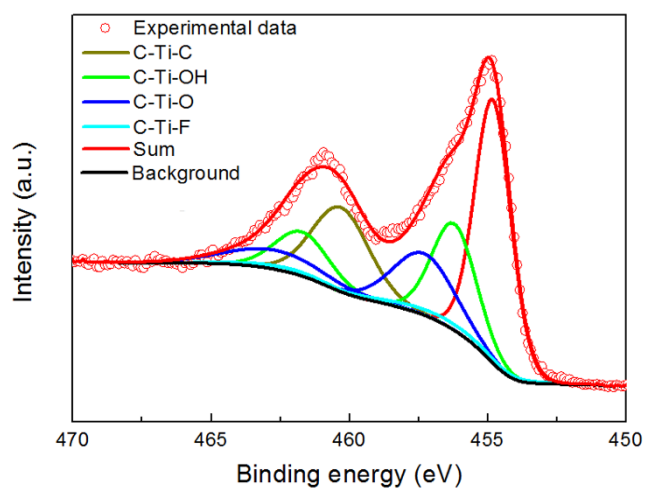


Fig. S3. X-ray photoelectron spectrum of $\text{Ti}_3\text{C}_2\text{T}_x$. The spectrum of Ti 2p is deconvoluted with C–Ti–C, C–Ti–OH, C–Ti–O, C–Ti–F bonding.

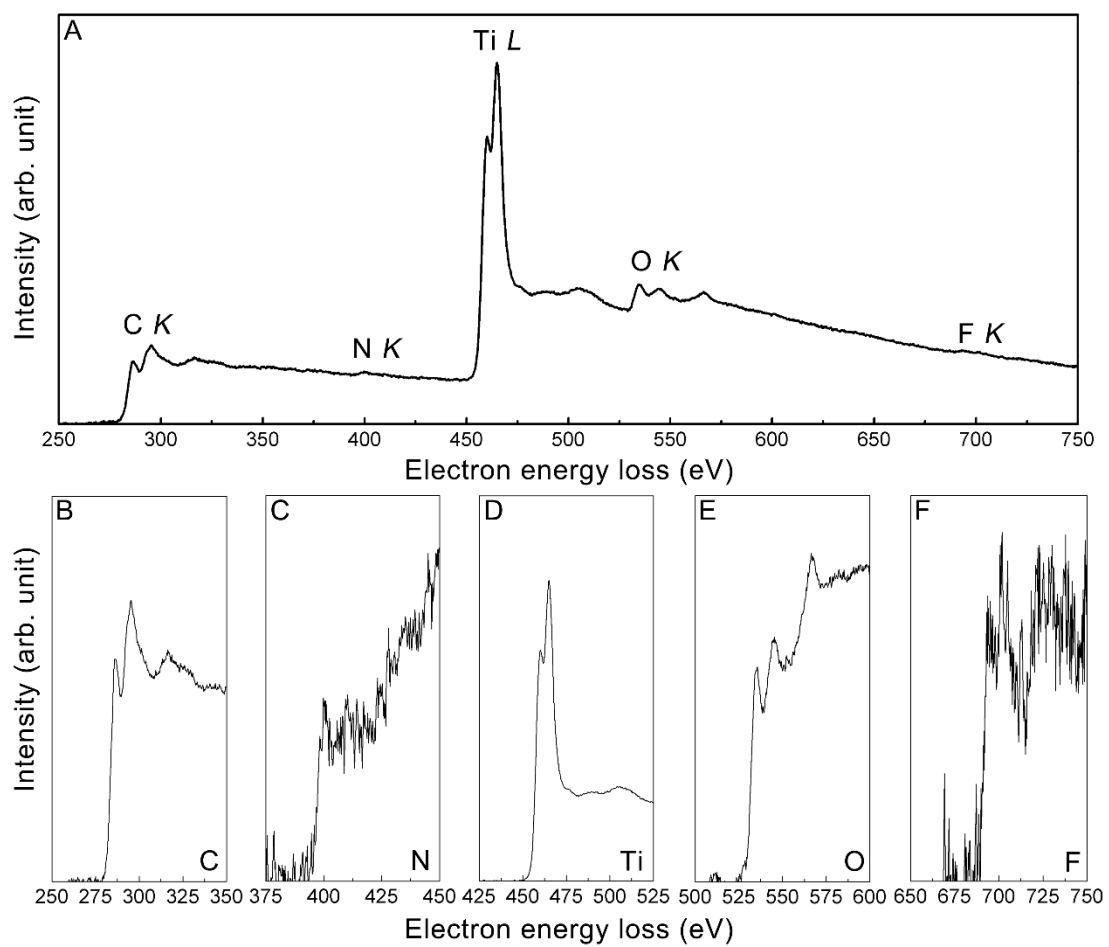


Fig. S4. EELS spectrum of $\text{NH}_3\text{-Ti}_3\text{C}_2\text{T}_x$. (A) Whole spectrum with elemental peaks labeled. (B–F) Extracted edges of C, N, Ti, O and F.

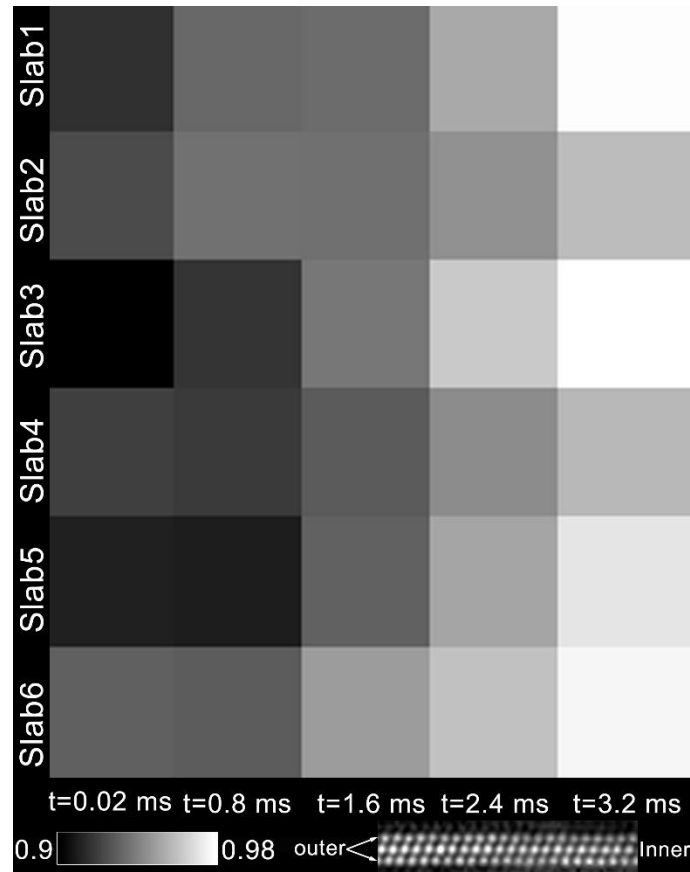


Fig. S5. Intensity ratio of the outer to the inner Ti column in Ti_3C_2 slabs. The ratio variations versus irradiation time of six slabs are presented. The local dose rate is $1.25 \times 10^9 \text{ e}^-/\text{\AA}^2\text{s}$ at 300 kV. To exclude the influence of Ti vacancies generated by HF etching, regions with the most homogenous intensity of Ti columns within the Ti_3C_2 slabs were chosen for analysis. It can be seen that the electron irradiation hardly decreases the ratio, indicating that the Ti vacancies produced by electron irradiation in the outer Ti columns are compensated by the Ti atoms in the inner Ti columns in a speed much faster than the temporal resolution of the microscope system.

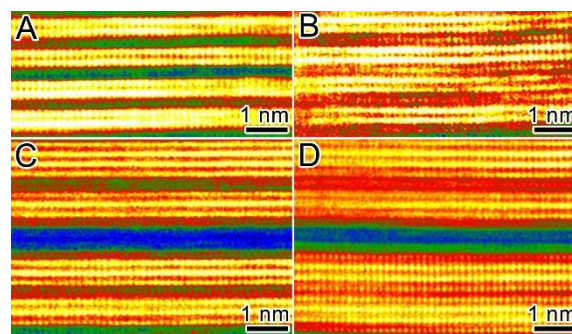


Fig. S6. Electron irradiation of Nb_4C_3 -MXene, $(\text{Ti}_{0.5}\text{Nb}_{0.5})_2\text{C}$ -MXene. Atomic-resolution HAADF-STEM images of (A,B) $(\text{Ti}_{0.5}\text{Nb}_{0.5})_2\text{C}$ -MXene and (C,D) Nb_4C_3 -

MXene (A,C) before and (B,D) after irradiation for (B) 2.8 ms and (D) 4.2 ms with a local dose rate of $1.6 \times 10^8 \text{ e}^-/\text{\AA}^2\text{s}$. The images are presented with a rainbow color-scale. Significant enhancement of the brightness of the functional group slabs between the carbide slabs indicates that Nb/Ti atoms migrate there from Nb_4C_3 and $(\text{Ti}_{0.5}\text{Nb}_{0.5})_2\text{C}$ slabs.

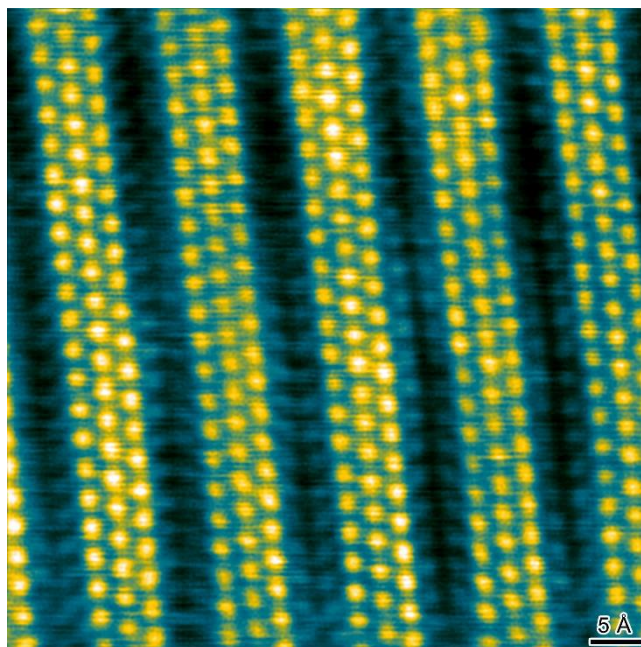


Fig. S7. Electron irradiation at 80 kV. Atomic-resolution HAADF-STEM image of $\text{NH}_3\text{-Ti}_3\text{C}_2\text{T}_x$ after irradiated for ~ 1.5 ms. The local dose rate on each pixel is $1.25 \times 10^9 \text{ e}^-/\text{\AA}^2\text{s}$. The image is presented with an aquatic color-scale. The significant intensity of the functional group slabs between the carbide slabs indicates that Ti atoms migrate there from Ti_3C_2 slabs.

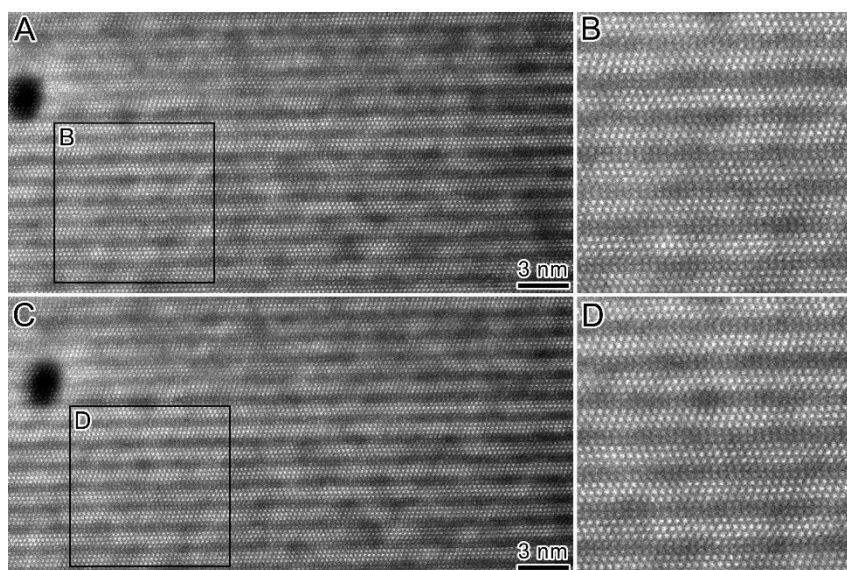


Fig. S8. Irreversible crystal restructuring. (A,B) Raw atomic-resolution HAADF-STEM image of $\text{NH}_3\text{-Ti}_3\text{C}_2\text{T}_x$ after 3 ms electron exposure with a local dose rate of $1.25 \times 10^9 \text{ e}^-/\text{\AA}^2\text{s}$ on each pixel. The same region was re-examined after one week, and presented in (C,D). (B,D) are enlarged images of the region outlined in (A,C). The relative intensity of the T_x slabs with respect to the Ti_3C_2 slabs generally remain unchanged, indicating that the Ti atoms residing in the T_x slabs do not go back to their original sites in the Ti_3C_2 slabs even after one-week duration.

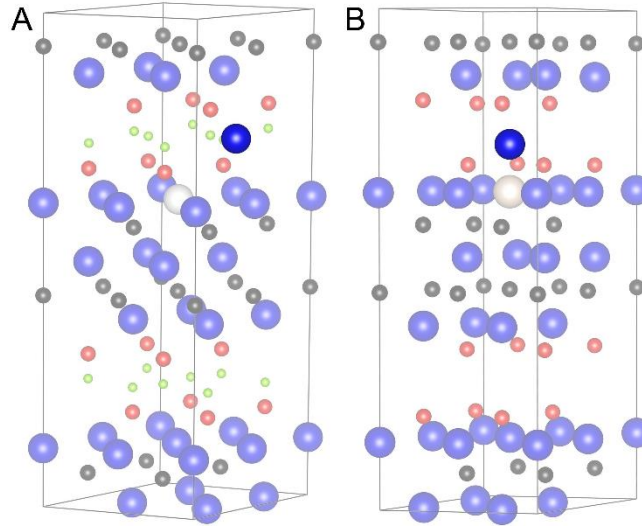


Fig. S9. Unit cell for Ti hopped structure. The lowest-energy configuration of Ti hopped to (A) Ti_F in $\text{Ti}_3\text{C}_2(\text{OH})_2$ and (B) Ti_{Fa} in $\text{Ti}_3\text{C}_2\text{O}_2$. Blue, black and red balls denote Ti, C and O atoms respectively. The grey ball marks the original position of the hopped Ti atom, un-shadowed blue ball.

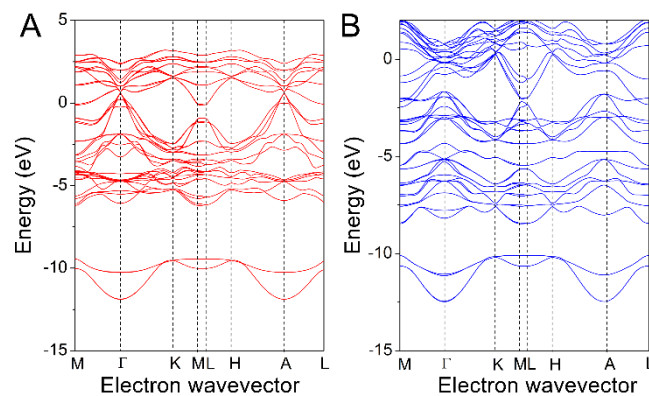


Fig. S10. Band structure of $\text{Ti}_3\text{C}_2\text{O}_2$ and $\text{Ti}_3\text{C}_2\text{O}_2\text{-Ti}_{Fa}$. Energy band structure of (A) $\text{Ti}_3\text{C}_2\text{O}_2$ and (B) $\text{Ti}_3\text{C}_2\text{O}_2\text{-Ti}_{Fa}$. The bands above Fermi level are drastically shifted downwards with the Ti_{Fa} sites occupied by Ti atoms.

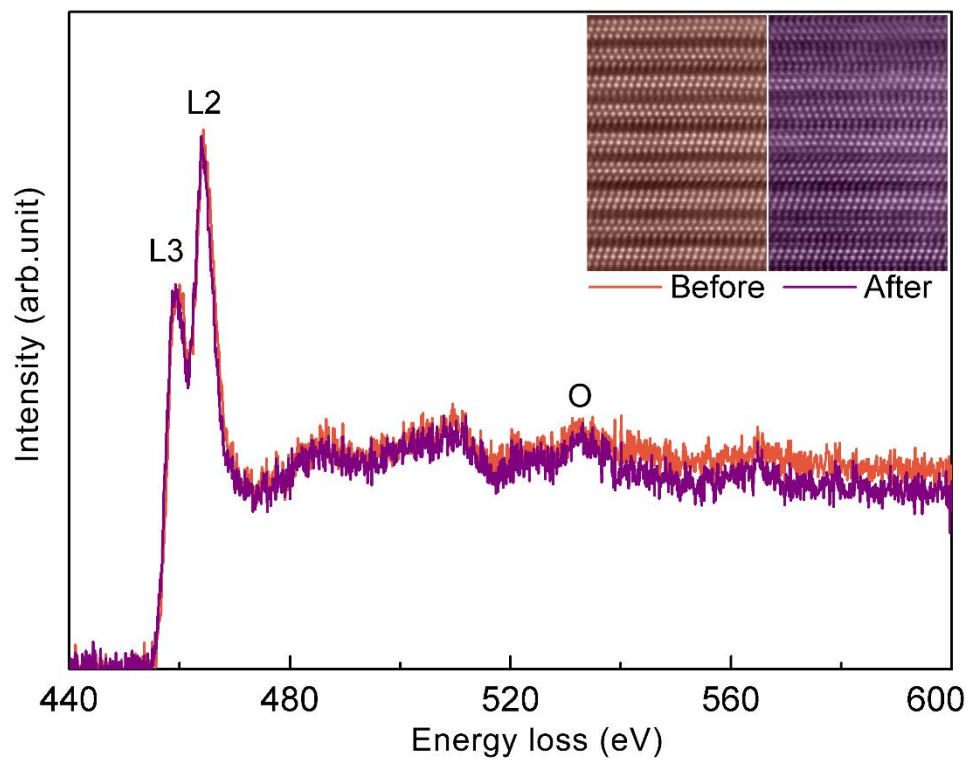


Fig. S11. Effect of electron irradiation on the EELS peaks of Ti and O in $\text{Ti}_3\text{C}_2\text{T}_x$. EELS peaks of Ti and O before (orange) and after (purple) electron irradiation. Inset: atomic-resolution HAADF-STEM images before (orange) and after (purple) irradiation.

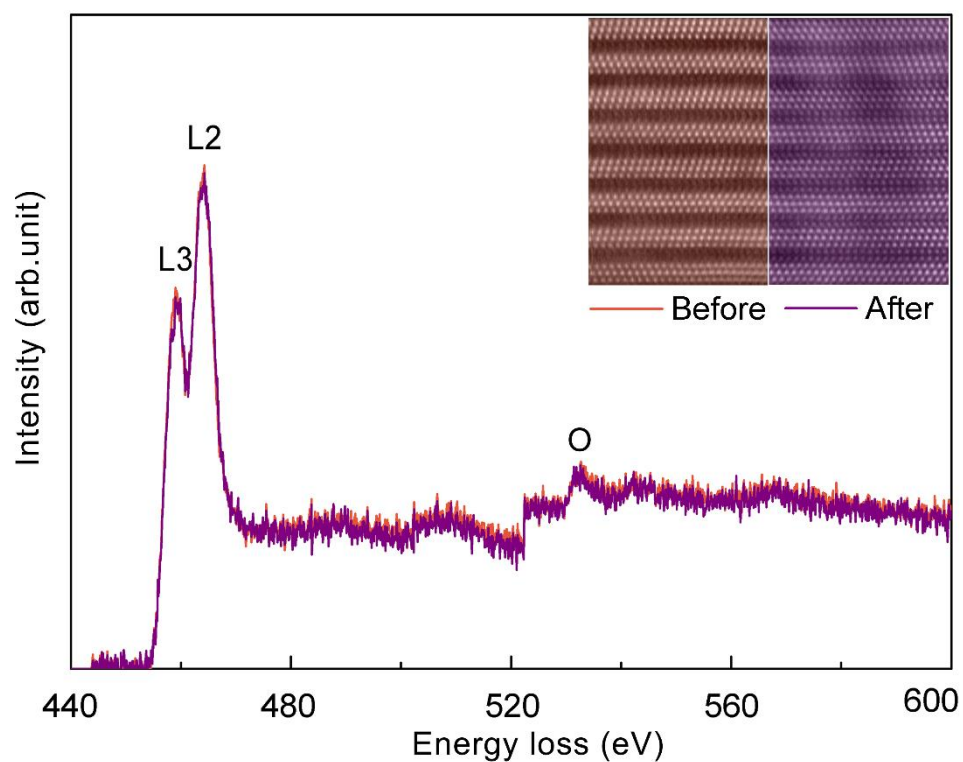


Fig. S12. Effect of electron irradiation on the EELS peaks of Ti and O in NH₃-Ti₃C₂T_x. EELS peaks of Ti and O before (orange) and after (purple) electron irradiation. Inset: atomic-resolution HAADF-STEM images before (orange) and after (purple) irradiation.